Acta Cryst. (1999). A**55**, 855–863

Diffraction of 100 to 200 keV X-rays from an $Si_{1-x}Ge_x$ gradient crystal: comparison with results from dynamical theory

Steffen Keitel,[a] Cécile Malgrange,[b] Thomas Niemöller[a] and Jochen R. Schneider[a]*

[a]*Hamburger Synchrotronstrahlungslabor HASYLAB at Deutsches Elektronen-Synchrotron DESY, Notkestrasse 85, D-22603 Hamburg, Germany, and* [b]*Laboratoire de Minéralogie-Cristallographie, associé au CNRS, Universités Pierre et Marie Curie (Paris 6) et Paris 7, Case 115, 4 place Jussieu, F-75252 Paris CEDEX 05, France. E-mail: schneider@desy.de*

(*Received 30 August 1998; accepted 22 February 1999*)

Abstract

In a large Czochralski-grown $Si_{1-x}Ge_x$ ($0.02 \leq x \leq 0.07$) gradient crystal, diffraction patterns have been measured in symmetrical Laue geometry using synchrotron radiation in the energy range 100–200 keV. The experimental data are in very good agreement with the results from geometrical optics theory for distorted crystals, if the creation of new wavefields for strain gradients larger than a critical value is taken into account. In this sense, the crystal behaves like an ideal gradient crystal. If the normal absorption is disregarded, for reflection 111 and 100 keV energy, the full width at half-maximum values and the peak reflectivities of the diffraction patterns range from 14.6″ and 97%, respectively, to 70.9″ and 74%, respectively, for a variation in the Ge concentration from 3.5 to 5.3 at.%.

1. Introduction

Recently, large $Si_{1-x}Ge_x$ gradient crystals have been grown (Abrosimov *et al.*, 1996), which offer new possibilities for optical elements in synchrotron-radiation instrumentation (Erko *et al.*, 1996). For high-energy synchrotron radiation, these crystals show diffraction patterns in transmission geometry that are about 50 times broader than those obtained for perfect crystals and with peak reflectivities of almost 100%, disregarding normal absorption (Keitel *et al.*, 1998). They are therefore very well suited for use as monochromators and analysers on triple-crystal diffractometers at photon energies above 80 keV. In order to understand the diffraction mechanism in these crystals, diffraction patterns have been measured in transmission geometry for reflections 111 and 333, using synchrotron radiation with energies between 100 and 200 keV. The crystal was 7 mm thick and the Ge concentration varied between 4 and 6% over a sample length of 40 mm. This concentration gradient causes a significant curvature of the lattice planes, like in a crystal subject to a thermal gradient. The measured rocking curves have been analysed using the geometrical dynamical diffraction theory for weakly distorted crystals and taking into account the creation of new wavefields in highly distorted crystals. Although the crystals are of very high quality, effectively they may behave like strongly distorted crystals because of the large extinction length and the narrow Darwin width for high-energy X-rays.

The paper is organized as follows. After a short description of the gradient crystal (§2) and the experimental setup for measuring the rocking curves (§3), the experimental results are presented (§4). Next (§5), the dynamical theory for distorted crystals is discussed for the special conditions of X-rays of energies above 80 keV and the theoretical results are compared with the experimental data (§5.2).

2. $Si_{1-x}Ge_x$ gradient crystal

The crystal plate, of dimensions $52 \times 33 \times 7$ mm, was cut out of an $Si_{1-x}Ge_x$ ($0.02 \leq x \leq 0.07$) ingot of about 35 mm in diameter and 125 mm in length, which was grown along the [111] direction by the Czochralski technique (Abrosimov *et al.*, 1996). The sample geometry is indicated in Fig. 1. Absolute lattice parameters were determined by Keitel *et al.* (1998) at different positions of the $Si_{1-x}Ge_x$ crystal with an accuracy of 10^{-4} with respect to the well known Si lattice

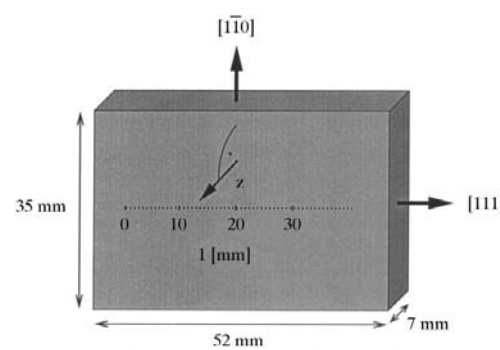

Fig. 1. Geometry of the $Si_{1-x}Ge_x$ gradient crystal. The Ge concentration gradient is parallel to [111].

parameter. These measurements were performed at the triple-crystal diffractometer at the HASYLAB high-field wiggler beamline BW5 using 120 keV synchrotron radiation. The Ge concentrations were determined from the measured lattice parameters using the calibration curve of Dismukes *et al.* (1964); the results are shown in Fig. 2.

On the other hand, starting from crystal-growth parameters, the variation of the Ge concentration in the crystal can be approximated by the Scheil–Pfann expression (Pfann, 1978),

$$C^{\bullet}_{\rm Ge} = C^{(0)}_{\rm Ge}(1-g)^{k-1} \quad \text{with} \quad C^{\rm cr}_{\rm Ge} = kC^{\bullet}_{\rm Ge}.$$

k represents the segregation coefficient, which for Ge in Si is less than 1. $g = M_{\rm cr}/M^{(0)}$ describes the solidified fraction, where $M_{\rm cr}$ represents the mass of the crystal and $M^{(0)}$ the mass of the melt in the crucible. $C^{\bullet}_{\rm Ge}$ is the varying Ge concentration in the melt, $C^{(0)}_{\rm Ge}$ the initial concentration in the melt, and $C^{\rm cr}_{\rm Ge}$ the Ge concentration in the crystal. In the range $0 < g < 0.6$, the Ge concentration in the crystal increases with a rather constant gradient because $k \simeq 0.35$. In the range $g > 0.6$, the Ge concentration increases with increasing g ratio. A fit of the Scheil–Pfann expression to the values of Ge concentration for the sample presently under consideration is also shown in Fig. 2. For another sample grown by this technique, the applicability of the Scheil–Pfann relation has been checked by an independent determination of the Ge concentration using infrared radiation (Abrosimov & Rossolenko, 1996). From the fitted Scheil–Pfann relation, the functional dependence of the reciprocal-lattice vector has been calculated, again using the calibration curve of Dismukes *et al.* (1964). The result is represented by the dotted curve in Fig. 2.

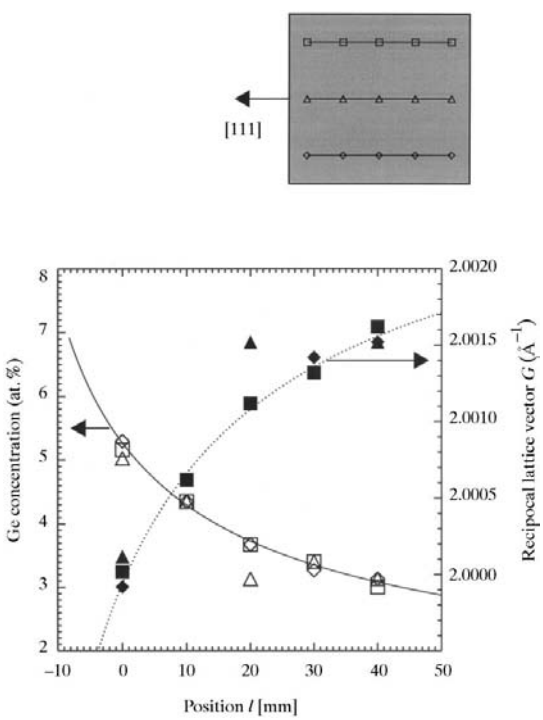

Fig. 2. Reciprocal-lattice vectors measured on an absolute scale for reflection 111 of the $Si_{1-x}Ge_x$ crystal in 15 different positions (see inset). The corresponding Ge concentrations shown as open symbols were determined by means of the calibration curve of Dismukes *et al.* (1964). The solid line represents a fit of the Scheil–Pfann relation to these Ge concentration data, from which the variation of the reciprocal-lattice vector was calculated (dotted line).

3. Experimental set-up

In order to measure the diffraction profiles for reflections 111 and 333, the diffractometer at the HASYLAB high-field wiggler beamline BW5 (Bouchard *et al.*, 1998) was operated in dispersion-free two-crystal mode using 100, 120, 160 and 200 keV synchrotron radiation. The monochromator was a perfect Si crystal also diffracting in transmission geometry. The cross section of the incident beam was 0.5 × 0.5 mm. As indicated in Fig. 3, the diffracted and the transmitted intensities, $I_r(\Delta\theta)$ and $I_t(\Delta\theta)$, have been measured as a function of rocking angle $\Delta\theta$. In order to eliminate the effect of absorption in the discussion of the diffraction properties of the sample, the reflectivity $r(\Delta\theta)$ is obtained by normalizing $I_r(\Delta\theta)$ with $I_t^{(0)} = I_0 \exp[-\mu t/\cos(\theta_B)]$, where μ is the absorption coefficient, t the sample thickness and θ_B the Bragg angle. The measured peak reflectivity is then defined by $r_m^{\rm max} = I_r^{\rm max}/I_t^{(0)}$. For 100 keV photons, the measured attenuation coefficient $\exp[-\mu t/\cos(\theta_B)]$ was 0.71, which reflects the high penetration power of high-energy synchrotron radiation in matter.

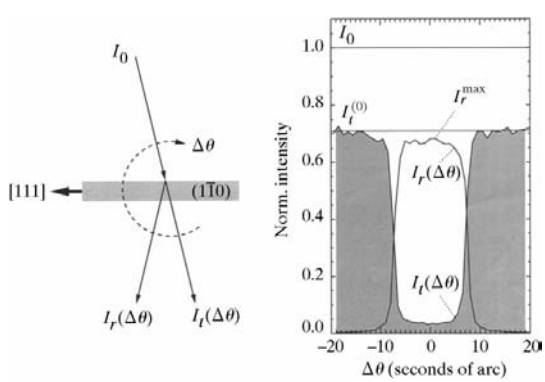

Fig. 3. The quantities measured in transmission geometry in a dispersion-free double-crystal setting using synchrotron radiation with energies between 100 and 200 keV. The monochromator is a perfect silicon crystal and the sample is the $Si_{1-x}Ge_x$ gradient crystal. I_0 represents the incident intensity, $I_t(\Delta\theta)$ the transmitted intensity and $I_r(\Delta\theta)$ the reflected intensity. $\Delta\theta$ is the rocking angle.

4. Experimental results

Fig. 4 shows the diffracted and transmitted intensities as a function of rocking angle $\Delta\theta$ measured for reflection 111 in the volume element at position $l = 30$ mm in the centre of the crystal using 100, 120, 160 and 200 keV synchrotron radiation. The peak reflectivities approach values close to 1 and they decrease with increasing photon energy. By contrast, Ω, the full width at half-maximum (FWHM) of the diffraction pattern, is independent of energy. For comparison, the FWHM values of the diffraction patterns measured with two perfect Si crystals in dispersion-free setting amount to 1.079, 0.898, 0.674 and 0.540″ for the four different photon energies, respectively. The shape of each diffraction pattern of the $Si_{1-x}Ge_x$ gradient crystal is almost rectangular and, on comparison with theory, each is found to be sufficiently well characterized by its FWHM, Ω, and the value of the average peak reflectivity $r_m^{\max}$. These observations are even more pronounced in the diffraction patterns measured for the same volume element for reflection 333, as shown in Fig. 5. Similar measurements have been performed in three additional volume elements of the crystal with increasing amounts of Ge. The results of all measurements made for reflection 111 in the central part of the crystal plate are summarized in Fig. 6. In the following, the increase of the FWHM of the diffraction patterns with increasing Ge content and the fact that it is independent of the photon energy will be explained by means of dynamical theory for distorted crystals.

Together with the high reflectivity, the rectangular shape of the diffraction pattern and the variation of its FWHM by simply translating the crystal in the beam is of great advantage when using $Si_{1-x}Ge_x$ gradient crystals as the monochromator or analyser on triple-crystal diffractometers for high-energy synchrotron radiation (Retsch *et al.*, 1998).

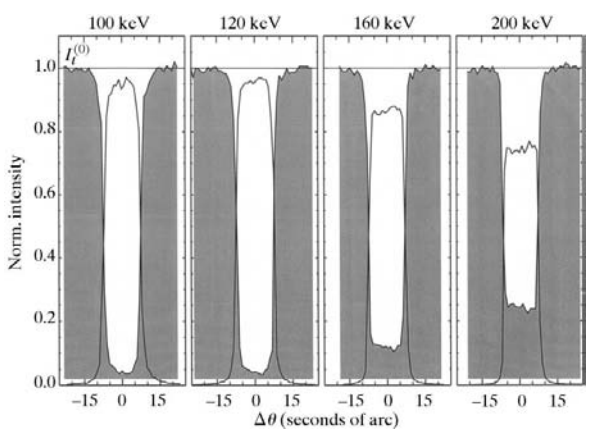

Fig. 4. Diffracted and transmitted intensities as a function of rocking angle measured for reflection 111 in position $l = 30$ mm in the centre of the crystal using 100, 120, 160 and 200 keV synchrotron radiation. The transmitted intensity $I_t^{(0)}$ was normalized to 1.

5. Interpretation of experimental data

Penning & Polder (1961) and Kato (1963, 1964*a*,*b*) have developed independently a geometrical optics theory of the propagation of X-rays in distorted crystals. Their theories lead to the same results and will be called PPK theory or geometrical theory hereinafter. They show that wavefields, which in perfect crystals propagate along straight beam paths, follow curved paths in distorted crystals, analogous to the propagation of light in a medium with a gradient in the index of refraction.

The basic parameter introduced in PPK theory to describe the distortion of the reflecting planes is the strain gradient β, defined as

$$\beta = [\Lambda_L/\cos^2(\theta_B)][\partial^2(\mathbf{h}\cdot\mathbf{u})/\partial s_0 \partial s_h], \qquad (1)$$

where $\mathbf{u}$ is the displacement vector of the atom from its ideal position, $\mathbf{h}$ the reciprocal-lattice vector, s_0 and s_h the coordinates along the directions of the incident and the reflected beam, respectively, θ_B the Bragg angle and Λ_L the inverse of the diameter of the dispersion surface, which is equal to the extinction length in the symmetrical Laue case:

$$\Lambda_L = \pi V \cos(\theta_B)/r_e\lambda|C|(F_h F_{\bar{h}})^{1/2}. \qquad (2)$$

V is the volume of the crystal unit cell, F_h and $F_{\bar{h}}$ are the structure factors for reflections h and $\bar{h}$, C represents the polarization factor, λ the wavelength of the X-rays and r_e the classical electron radius. It is important to point out that the parameter β, which describes the effective distortion of the crystal, is proportional to the extinction length Λ_L, *i.e.* inversely proportional to the wavelength and the structure factor. Therefore, the higher the photon energy is and the smaller the structure factor is, the higher the effective distortion is. As a consequence, a crystal of relatively high degree of perfection may behave like a highly distorted crystal for the diffraction of short-wavelength photons.

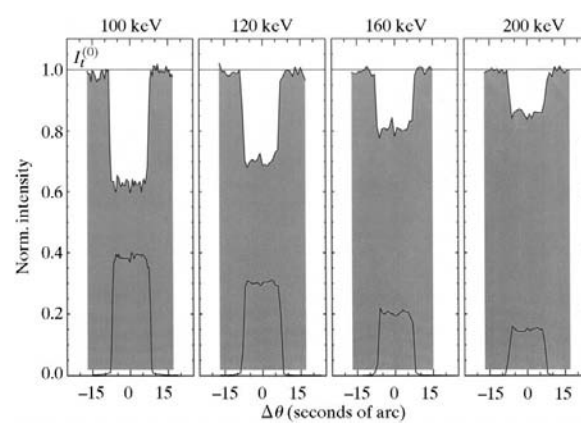

Fig. 5. Diffracted and transmitted intensities as a function of rocking angle measured for reflection 333; same conditions as Fig. 4.

The geometrical theory no longer applies when the strain gradient is too high. Authier & Balibar (1970) had first shown that it is valid as far as the variation of the departure from the Bragg angle along a distance equal to the extinction length is much less than the width of the diffraction pattern of a perfect crystal, the so-called Darwin width; otherwise a new wavefield is created. Numerical simulations based on Takagi–Taupin equations, which are valid for high values of the strain gradient β, have shown that the new wavefield is created for $|\beta| > \pi/2\Lambda_L$ in the region of the crystal where the Poynting vector is parallel to the reflecting planes (Balibar *et al.*, 1975). For some special cases, the authors give numerical values of the intensity related to the new wavefield. Later it was demonstrated analytically by Balibar *et al.* (1983), for Laue geometry, and by Chukhovskii & Malgrange (1989), for Bragg geometry, that, in the case of a constant strain gradient β, the fraction of the intensity that is transferred to the new wavefield is equal to

$$\exp(-2\pi\beta_c/|\beta|) \quad \text{with} \quad \beta_c = \pi/2\Lambda_L. \tag{3}$$

It is interesting to note that

$$\beta_c/|\beta| \propto 1/\Lambda_L^2 \propto \lambda^2 F_h F_{\bar{h}},$$

i.e. in a crystal of given strain the probability that intensity is transferred to these new wavefields increases strongly for shorter wavelength radiation. In the case of a variable strain gradient β, Gronkowski & Malgrange (1984) have shown by means of numerical simulations that the creation of the new wavefield occurs where the bent beam path is parallel to the lattice plane, and that the fraction of the intensity that is transferred to this new wavefield is still given by $\exp(-2\pi\beta_c/|\beta|)$, with β being taken at the point where the new wavefield is created. In summary, it is possible to describe X-ray propagation in slightly and highly distorted crystals by means of the geometrical theory with the additional condition of taking the creation of new wavefields into account. In the following, these general theoretical results will be adapted to the special case of the diffraction of X-rays with energies between 100 and 200 keV from an $Si_{1-x}Ge_x$ gradient crystal in symmetrical Laue geometry.

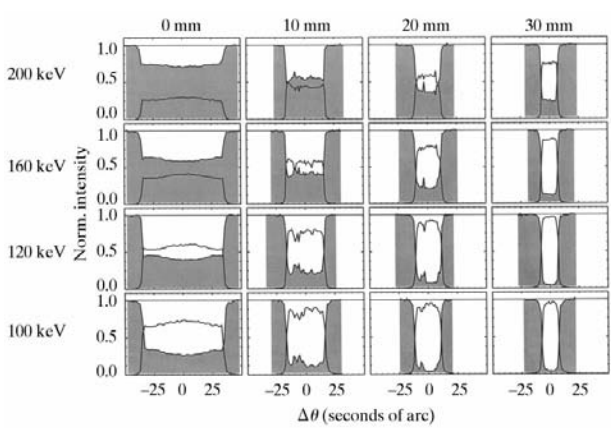

Fig. 6. Diffracted and transmitted intensities as a function of rocking angle measured for reflection 111 in position $l = 0$, 10, 20 and 30 mm in the centre of the crystal using 100, 120, 160 and 200 keV synchrotron radiation. The transmitted intensity $I_t^{(0)}$ was normalized to 1.

5.1. *Qualitative picture*

Before considering PPK theory, some results of the dynamical theory for the diffraction of X-rays from perfect crystals in symmetrical Laue geometry are recalled. As indicated in Fig. 7, an incident plane wave with wave vector **MO**, which deviates from the Bragg angle by $\Delta\theta$, excites two wavefields in the crystal with tie points P_1 and P_2 on the two branches of the dispersion surface. Inside the crystal, the wavefields propagate along straight beam paths parallel to their Poynting vectors $\mathbf{S}_1$ and $\mathbf{S}_2$, which are normal to the dispersion surface at P_1 and P_2, respectively, and symmetric with respect to the lattice planes. The Poynting vector $\mathbf{S}_i$ $(i = 1, 2)$ may be expressed by

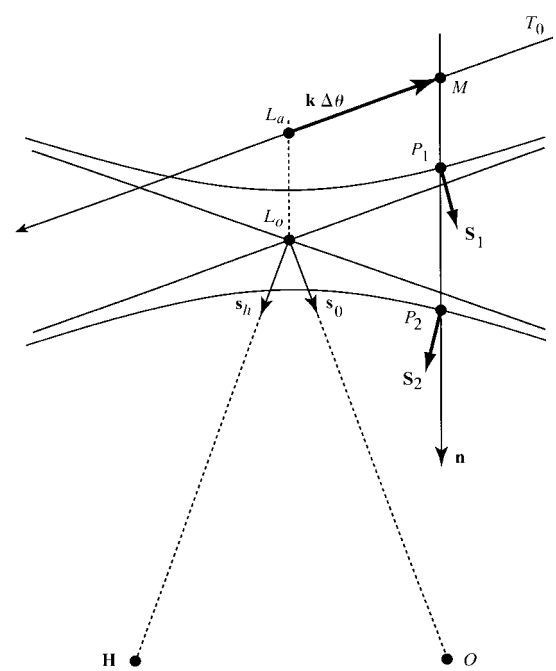

Fig. 7. Schematic view of the dispersion surface and the boundary conditions for symmetric Laue geometry. O is the origin of the reciprocal lattice and **H** the reciprocal-lattice vector. $\mathbf{s}_0$ and $\mathbf{s}_h$ represent the unit vectors in the directions of the incident and the diffracted beam, respectively. **MO** represents the wave vector of the incident wave, L_a the Laue and L_o the Lorentz point. $k\Delta\theta$ corresponds to the deviation of the incident beam from the exact Bragg condition, **k** being the wave vector in vacuum. $\mathbf{S}_1$ and $\mathbf{S}_2$ are the Poynting vectors at tie points P_1 and P_2 on the dispersion surface.

$$\mathbf{S}_i \propto (|D_{0i}|^2\mathbf{s}_0 + |D_{hi}|^2\mathbf{s}_h), \quad (4)$$

where D_{0i} and D_{hi} represent the amplitudes of the waves forming wavefield i, and $\mathbf{s}_0$ and $\mathbf{s}_h$ are the unit vectors along the incident and reflected beam directions, respectively.

The splitting of the intensity between wavefield 1 and wavefield 2 at the entrance surface results from applying boundary conditions to the electric field vectors. One finds that the intensity is higher in the wavefield with a Poynting vector closer to $\mathbf{s}_0$; the ratio of the two wavefield intensities increases with increasing angle between the Poynting vector and the reflecting net planes. At the exit surface of the crystal, a given wavefield splits into a reflected and a transmitted wave. Their intensities are again given through boundary conditions and one finds that the higher the reflected (transmitted) beam intensity is, the closer the direction of the Poynting vector is to $\mathbf{s}_h$ ($\mathbf{s}_0$).

When the crystal is rotated, the point M moves along the line T_0 crossing the Laue point L_a, which corresponds to the exact Bragg condition, and the tie points P_1 and P_2 move along the dispersion surface through its centre. For an incident wave far from the Bragg condition, the Poynting vectors $\mathbf{S}_1$ and $\mathbf{S}_2$ are almost parallel to $\mathbf{s}_0$ and $\mathbf{s}_h$ on one side of the Bragg peak, and to $\mathbf{s}_h$ and $\mathbf{s}_0$ on the other side. In both cases, all the intensity is transferred to the wavefield parallel to $\mathbf{s}_0$. Because in this limiting case the Poynting vector at the exit surface is parallel to $\mathbf{s}_0$, one obtains only a transmitted wave. This is expected intuitively since, far from Bragg incidence, the X-ray beam passes straight through the crystal and is only affected by normal absorption.

For the weakly distorted crystal, PPK theory demonstrates that the curvature of the beam paths during wavefield propagation is due to a movement of the tie points along the dispersion surface, *i.e.* in Fig. 8 from points P_1 and P_2 at the crystal entrance surface to points P_1' and P_2' at its exit surface. For a constant strain gradient β, as realized in the case of lattice planes bent with a constant radius of curvature, the projection of P_1P_1' and P_2P_2' on a line parallel to the reciprocal-lattice vector $\mathbf{h}$ is proportional to βt, where t represents the thickness of the crystal. The tie points P_1 and P_2 are determined by the direction of the incident beam, whereas the tie points P_1' and P_2' are determined by the strain gradient β, *i.e.* the radius of curvature of the lattice planes for the example considered here. Therefore, as indicated in Fig. 8, the beam trajectories related to the two wavefields will in general not meet at the crystal exit surface.

For larger values of the effective distortion, but still $|\beta| < \beta_c$, which in the case of high photon energies occurs in rather perfect crystals, the curvature of the trajectory is much stronger because, as indicated in Fig. 9, the diameter of the dispersion surface is smaller, *i.e.* the angular range in which the dispersion surface deviates significantly from the asymptotes perpendicular to $\mathbf{s}_0$ and $\mathbf{s}_h$ is much smaller. The tilt of the beam path shown in Fig. 8 now occurs in a very localized area of the crystal and the turning of the beam trajectory is more kink like. Boundary conditions can be applied at the entrance and exit surfaces in the same manner as in the case of a perfect crystal. At the entrance surface, one wavefield starts propagation parallel to $\mathbf{s}_0$, the other parallel to $\mathbf{s}_h$, and all the intensity is transferred to the first wavefield. During propagation of this wavefield, the tie point moves on the dispersion surface and at the exit surface the wavefield propagates in a direction parallel to $\mathbf{s}_h$, *i.e.* all its intensity is transferred to the reflected beam. Since most of the trajectory inside the crystal is parallel either to $\mathbf{s}_0$ or to $\mathbf{s}_h$, the Borrmann effect does

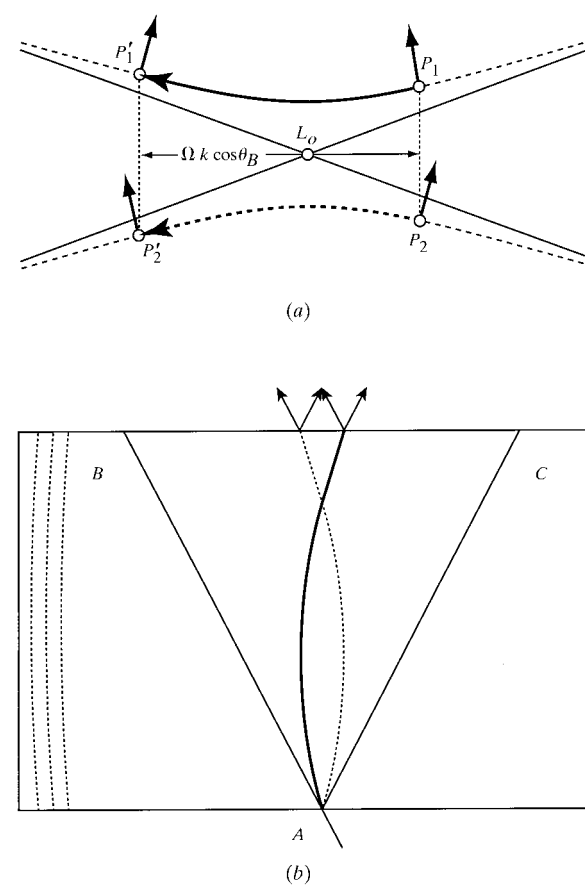

Fig. 8. Schematic representation of the dispersion surface and the energy flow in a weakly distorted crystal diffracting in symmetrical Laue geometry. The direction of the energy flow of the two wavefields at the entrance and the exit surface is given by the direction of the Poynting vectors at tie points P_1 and P_1' for wavefield 1 and P_2 and P_2' for wavefield 2. The width of the diffraction pattern $\Omega = \beta t(\delta/2)$ is determined by the Darwin width δ, the strain gradient β and the thickness t of the gradient crystal; in the present case, to a good approximation it is equal to the angle between the lattice-plane orientation at the entrance and that at the exit surface of the crystal. ABC defines the Borrmann triangle.

not occur and the wavefield is affected by normal absorption only. Finally, if one neglects absorption completely, all the incident intensity is transferred to the reflected beam.

As mentioned before for strongly distorted crystals with $|\beta| > \beta_c$, the creation of new fields at the kink-like turning region of the beam trajectory has to be taken into account, which leads to a reduction of the diffracted intensity.

5.2. *Comparison with experimental data*

As is usual in dynamical theory, the positions of the tie points P_i on the dispersion surfaces are described by means of the dimensionless parameter η. For P_1, the tie point at the entrance surface, one obtains

$$\eta_i = 2\Delta\theta/\delta, \tag{5}$$

where δ represents the Darwin width,

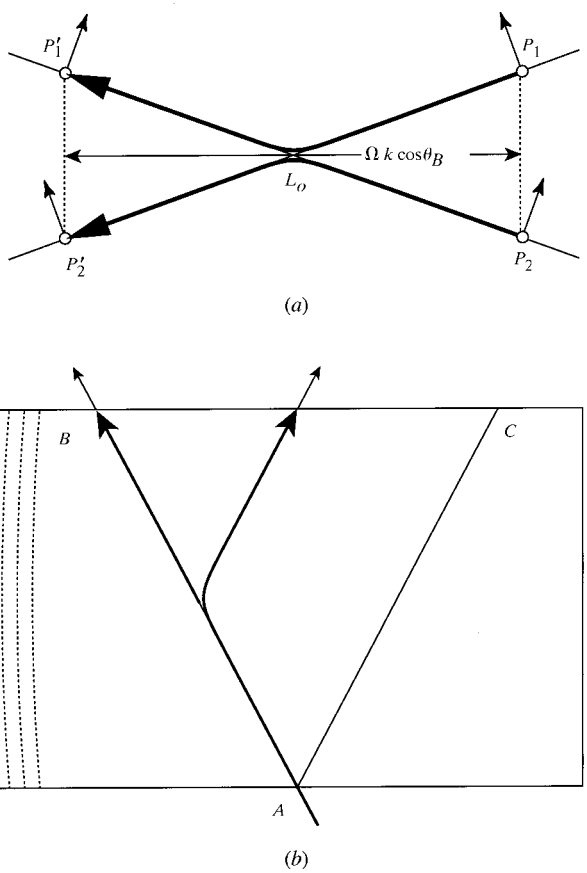

Fig. 9. Schematic representation of the dispersion surface and the energy flow in the same weakly distorted crystal as presented in Fig. 8, but for much shorter wavelength. Because of the smaller diameter of the dispersion surface, the tilt in the trajectory of the energy flow is localized in the crystal and is more kink like. All intensity is shifted into the diffracted beam direction.

$$\delta = 2d_{hkl}/\Lambda_L, \tag{6}$$

with d_{hkl} representing the lattice-plane spacing for reflection hkl. $\Delta\theta$ describes the inclination of the lattice-plane orientation from the exact Bragg condition. In general, η values are transformed into angles in wave-vector space by multiplication by $\delta/2$; examples are given in Figs. 8 and 9.

PPK theory shows that the local value $\eta(z)$ at a depth z in the crystal is equal to

$$\eta(z) = \eta_i + \beta z.$$

The η parameter at the exit surface is thus given by

$$\eta_e = \eta_i + \beta t. \tag{7}$$

The kink in the beam trajectory (see Fig. 9) occurs at depth z where $\eta = 0$. Then, for all η_i values with $-\beta t < \eta_i < 0$, the beam trajectory shows such a kink and, as explained above, the incident intensity is fully transferred to the reflected beam, neglecting absorption. For the limiting values $\eta_i = -\beta t$ and $\eta_i = 0$, the trajectories either start or leave the crystal parallel to the reflecting planes and, owing to the usual boundary conditions in dynamical theory, the reflected intensity is half the maximum value. For $\eta_i = 0$, half the intensity is transferred to the wavefield that ends parallel to $\mathbf{s}_h$. For $\eta_i = -\beta t$, all the intensity is transferred to one wavefield, but at the exit surface only half the intensity is transferred to the reflected beam. As indicated in Fig. 9, the FWHM of the diffraction pattern expressed in dimensionless η units is then equal to $|\beta|t$, and transformed into angular units using equation (5):

$$\Omega = |\beta|t(\delta/2). \tag{8}$$

In the present case, because of the smallness of the Bragg angle θ_B, $\partial^2/\partial s_0 \partial s_h \cong \cos^2(\theta_B)\partial^2/\partial z^2$ is a very good approximation, where z represents a coordinate normal to the crystal surface. Using equations (1) and (6), one obtains

$$\Omega = [\partial^2(\mathbf{h}\cdot\mathbf{u})/\partial z^2]d_{hkl}t,$$

which is independent of wavelength and structure factor, as well as of the order of the reflection, because $|\mathbf{h}|$ is proportional to $1/d_{hkl}$. Ω, the FWHM of the diffraction pattern of the distorted crystal, only depends on the strain in the sample. The experimental results, summarized in Table 1, confirm this statement. Within $\pm 3\%$, the Ω values are, indeed, independent of energy and order of reflection. With the Ω value measured in the four different volume elements of the sample containing a known amount x of Ge atoms (see Fig. 2), the strain parameter β can be calculated from equations (8), (2) and (6). The calculation of the structure factor F_h was based on an average form factor

$$\langle f \rangle = x f_{\mathrm{Ge}} + (1-x) f_{\mathrm{Si}}.$$

The form-factor values f_{Ge} and f_{Si} for germanium and silicon were taken from *Pendellösung* measurements by

Table 1. *Full width at half-maximum values and experimental and calculated peak reflectivities for the $Si_{1-x}Ge_x$ crystal*

The FWHM of each diffraction pattern, Ω ($''$), the values $r_m^{\max}$ measured for reflections 111 and 333 at four different positions along the Ge gradient in the centre of the $Si_{1-x}Ge_x$ crystal, using 100, 120, 160 and 200 keV synchrotron radiation, and the corresponding calculated average peak reflectivities, $r_{\rm calc}^{\max}$, are listed, along with the average FWHM of the diffraction patterns, $\langle\Omega\rangle$, measured in a given volume element of the crystal for the two reflections with the four different photon energies.

		0 mm	10 mm	20 mm	30 mm
Reflection 111					
200 keV	Ω	70.5	33.8	21.2	14.2
	$r_m^{\max}$	0.30	0.50	0.65	0.77
	$r_{\rm calc}^{\max}$	0.28	0.48	0.64	0.78
160 keV	Ω	70.4	32.9	21.4	14.5
	$r_m^{\max}$	0.42	0.62	0.80	0.88
	$r_{\rm calc}^{\max}$	0.40	0.64	0.80	0.90
120 keV	Ω	70.2	32.7	22.4	15.2
	$r_m^{\max}$	0.61	0.81	0.93	0.97
	$r_{\rm calc}^{\max}$	0.59	0.835	0.94	0.98
100 keV	Ω	70.3	33.9	22.8	14.6
	$r_m^{\max}$	0.74	0.90	0.96	0.97
	$r_{\rm calc}^{\max}$	0.73	0.93	0.98	0.997
Reflection 333					
200 keV	Ω	70.9	34.5	19.6	14.4
	$r_m^{\max}$	0.05	0.08	0.12	0.16
	$r_{\rm calc}^{\max}$	0.03	0.06	0.10	0.14
160 keV	Ω	70.7	34.7	20.8	13.9
	$r_m^{\max}$	0.06	0.11	0.17	0.22
	$r_{\rm calc}^{\max}$	0.05	0.10	0.15	0.21
120 keV	Ω	71.0	35.2	21.5	14.8
	$r_m^{\max}$	0.11	0.17	0.26	0.31
	$r_{\rm calc}^{\max}$	0.09	0.17	0.25	0.34
100 keV	Ω	72.8	35.6	21.7	15.2
	$r_m^{\max}$	0.13	0.24	0.32	0.40
	$r_{\rm calc}^{\max}$	0.12	0.23	0.34	0.45
	$\langle\Omega\rangle$	70.86 (83)	34.16 (103)	21.43 (98)	14.60 (46)

Deutsch *et al.* (1990) and Teworte & Bonse (1984), respectively.

In order to explain the observed energy dependence of the reflectivity, one has to take into account the creation of the new wavefields discussed above, which reduce the intensity of the reflected beam. The beam paths of the primary and of this new wavefield are symmetric with respect to the reflecting lattice planes (Fig. 9). The intensity related to the new wavefields is thus transferred into the transmitted-beam direction parallel to $\mathbf{s}_0$. Because the shape of each measured diffraction patterns is almost rectangular, it is sufficient to calculate an average peak intensity. As stated above, the fraction of the intensity that is transferred to the new wavefield is proportional to $\exp(-2\pi\beta_c/|\beta|)$, so that the intensity $I_{\max}$ of the plateau is calculated according to

$$I_{\rm calc}^{\max} = I_0 \exp[-\mu t/\cos(\theta_B)][1 - \exp(-2\pi\beta_c/|\beta|)], \quad (9)$$

where I_0 is the incident beam intensity. If $I_t^{(0)}$ is the transmitted intensity outside the angular range of the diffraction pattern, then

$$r_{\rm calc}^{\max} = I_{\max}/I_t^{(0)} = [1 - \exp(-2\pi\beta_c/|\beta|)]. \quad (10)$$

As demonstrated in Table 1, very good agreement is found between the experimental and the calculated peak reflectivities for all Ge concentrations, photon energies and orders of reflection considered.

It is interesting to calculate the integrated reflecting power for the limit of β towards infinity, which corresponds to the assumption made in the kinematical diffraction theory. By expanding the exponential function in equation (10), one obtains

$$r_{\rm calc}^{\max} = 2\pi\beta_c/|\beta|.$$

In the present case, the integrated reflecting power R is well approximated by the product of the FWHM of the diffraction pattern, Ω, and the peak reflectivity, $r_{\rm calc}^{\max}$. Together with equations (3), (6) and (8), one obtains

$$\begin{aligned} R &= r_{\rm calc}^{\max}\Omega \\ &= \pi\beta_c\delta t \\ &= \pi(\pi/2\Lambda_L)(2d_{hkl}/\Lambda_L)t \\ &= (\pi/\Lambda_L)^2 d_{hkl} t \\ &= (r_e^2/V^2)|C|^2 F_h F_{\bar{h}}[\lambda^3/\sin(2\theta_B)][t/\cos(\theta_B)] \\ &= R_{\rm kin}, \end{aligned}$$

which is identical to the expression for $R_{\rm kin}$ calculated from kinematical theory for transmission geometry.

Fig. 10 shows a quite systematic dependence of the reflectivities for the different photon energies and germanium concentrations on the reflections 111 and 333. The fact that saturation for photon energies of 100 keV is reached for reflection 111 should be emphasized. In the crystal volume element at position $l = 0$ mm, containing ~5.3 at.% Ge and showing the broadest diffraction pattern ($\Omega = 70.9''$), a big change in the reflectivity from $r_{\rm calc}^{\rm max} = 0.03$ (200 keV, reflection 333) to $r_{\rm calc}^{\rm max} = 0.73$ (100 keV, reflection 111) is observed for a change in extinction length from 802.1 to 219.7 μm. For the volume element at position $l = 30$ mm with the narrowest diffraction pattern ($\Omega = 14.6''$) and containing ~3.5 at.% Ge, a variation in extinction length from 826.8 to 226.4 μm leads to an increase of reflectivity from $r_{\rm calc}^{\rm max} = 0.14$ (200 keV, reflection 333) to $r_{\rm calc}^{\rm max} = 0.997$ (100 keV, reflection 111). Rather moderate changes in the extinction length obviously lead to strong variations in the crystal reflectivity.

In the discussion above, the strain parameter β is assumed to be constant along the beam path, *i.e.* along the direction normal to the crystal surface. Because of the smallness of the Bragg angle, this 'efficient strain parameter' is only due to the curvature of the lattice planes, and thus is inversely proportional to the radius of curvature. The value of the radius of curvature deduced from the different experimental β values varies between 20 m at sample position $l = 0$ mm and 100 m at $l = 30$ mm. These values are in very good agreement with those calculated from the lattice-parameter gradient. In another experiment, using the same scattering geometry and photon energy, the Borrmann fan was scanned with a 10 μm wide slit and the variation of the wavelength of the diffracted radiation was determined by means of dispersive analyser scans. From these data, the radius of curvature of the diffraction planes could be calculated. The resulting value is again in very good agreement with that calculated from the width of the corresponding diffraction pattern.

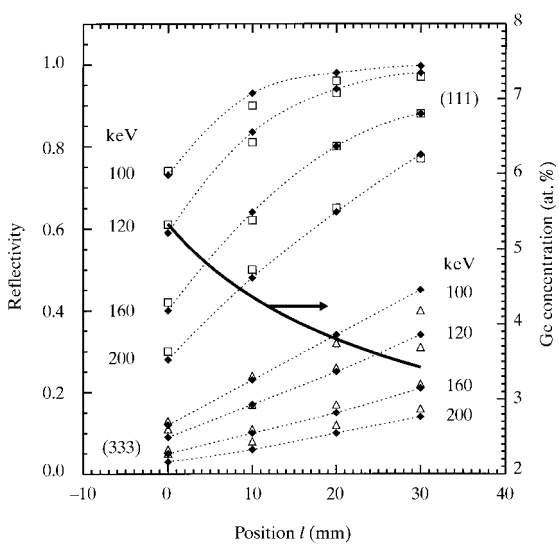

Fig. 10. Average peak reflectivities calculated (filled diamonds) and measured at four different positions along the Ge gradient in the centre of the $Si_{1-x}Ge_x$ crystal for reflections 333 (open triangles) and 111 (open squares) for photon energies of 100, 120, 160 and 200 keV. The full line represents the Ge concentration profile taken from Fig. 1.

6. Conclusions

The diffraction of photons with energies between 100 and 200 keV in an $Si_{1-x}Ge_x$ crystal investigated in symmetrical Laue geometry is well described by means of the geometrical optics (PPK) theory. If the modulus of the strain gradient β is larger than a critical value β_c, the creation of new wavefields has to be taken into account, which reduces the reflected intensity. It is important to realize that the ratio $\beta_c/|\beta|$ is proportional to $\lambda^2 F_h F_{\bar{h}}$, *i.e.* a given strain field which is weak for 1 Å radiation will act like a strong strain field for diffraction of 0.1 Å radiation. As expected from theory, the FWHM of the diffraction pattern measured in a given volume element of the sample, *i.e.* for a certain concentration of Ge atoms, does not depend on wavelength or structure factor and can therefore be used to determine the strain gradient β. With this input parameter, the measured reflectivity could be very well reproduced by theory over a wide range of reflectivities. In this sense, the studied $Si_{1-x}Ge_x$ crystal behaves like a perfect gradient crystal. For lower photon energies, a full calculation of the diffraction pattern should be performed and more detailed information on the strain gradient will be needed.

Thanks are due to N. V. Abrosimov and H. Riemann from the Institut für Kristallzüchtung in Berlin, Germany, for providing the crystal.

References

Abrosimov, N. V. & Rossolenko, S. N. (1996). 1996 Annual Report of Institut für Kristallzüchtung, Berlin, Germany.
Abrosimov, N. V., Rossolenko, S. N., Alex, V., Gerhard, A. & Schröder, W. (1996). *J. Cryst. Growth*, **166**, 657–662.
Authier, A. & Balibar, F. (1970). *Acta Cryst.* A**26**, 647–654.
Balibar, F., Chukhovskii, F. & Malgrange, C. (1983). *Acta Cryst.* A**39**, 387–399.
Balibar, F., Epelboin, Y. & Malgrange, C. (1975). *Acta Cryst.* A**31**, 836–840.
Bouchard, R., Hupfeld, D., Lippmann, T., Neuefeind, J., Neumann, H.-B., Poulsen, H. F., Rütt, U., Schmidt, T. & Schneider, J. R. (1998). *J. Synchrotron Rad.* **5**, 90–101.
Chukhovskii, F. & Malgrange, C. (1989). *Acta Cryst.* **45**, 732–738.
Deutsch, M., Hart, M. & Cummings, S. (1990). *Phys. Rev. B*, **42**, 1248–1253.

Dismukes, J. P., Ekstrom, L. & Paff, R. J. (1964). *J. Phys. Chem.* **68**, 3021–3027.
Erko, A., Schäfers, F., Gudat, W., Abrosimov, N. V., Rossolenko, S. N., Alex, V., Groth, S. & Schröder, W. (1996). *Nucl. Instrum. Methods Phys. Res. A*, **374**, 408–412.
Gronkowski, J. & Malgrange, C. (1984). *Acta Cryst.* A**40**, 515–522.
Kato, N. (1963). *J. Phys. Soc. Jpn*, **18**, 1785–1791.
Kato, N. (1964*a*). *J. Phys. Soc. Jpn*, **19**, 67–77.
Kato, N. (1964*b*). *J. Phys. Soc. Jpn*, **19**, 971–985.
Keitel, S., Retsch, C. C., Niemöller, T., Schneider, J. R., Abrosimov, N. V., Rossolenko, S. N. & Riemann, H. (1998). *Nucl. Instrum. Methods Phys. Res. A*, **414**, 427–430.
Penning, P. & Polder, D. (1961). *Philips Res. Rep.* **16**, 419.
Pfann, W. G. (1978). *Zone Melting*, 2nd ed., p. 11. New York: Robert E. Krieger.
Retsch, C. C., Keitel, S., Schulte-Schrepping, H., Schneider, J. R., Abrosimov, N. V., Rossolenko, S. N. & Riemann, H. (1998). *Proc. SPIE*, **3448**, 76–86.
Teworte, R. & Bonse, U. (1984). *Phys. Rev. B*, **29**, 2102–2108.